1

Criteria for the optimal selection of remote sensing optical images to map event landslides

4

5   Fiorucci F.[1], Giordan D.[2], Santangelo M.[1], Dutto F.[3], Rossi M.[1], Guzzetti F.[1]

6   1   Istituto di Ricerca per la Protezione Idrogeologica, Consiglio Nazionale delle Ricerche, via
7   della Madonna Alta 126, 06128 Perugia, Italy

8   2   Istituto di Ricerca per la Protezione Idrogeologica, Consiglio Nazionale delle Ricerche, Strada
9   delle Cacce 73, 10135 Torino, Italy

10 3   Servizio Protezione Civile della Città Metropolitana di Torino, Via Alberto Sordi 13, 10095
11   Grugliasco, Italy

12

13 Correspondence to: Federica Fiorucci (Federica.Fiorucci@irpi.cnr.it)

14

15

Abstract

We executed an experiment to determine the effects of optical image characteristics on event landslide mapping. In the experiment, we compared eight maps of the same landslide, the Assignano landslide, in Umbria, Central Italy. Six maps were obtained through the expert visual interpretation of monoscopic and pseudo-stereoscopic (2.5D), ultra-resolution (3×3 cm) images taken on 14 April 2014 by a Canon EOS M photographic camera flown by an CarbonCore 950 hexacopter over the landslide, and of monoscopic and stereoscopic, true-colour and false-colour-composite, 1.84×1.84 m resolution images taken by the WorldView-2 satellite also on 14 April 2014. The seventh map was prepared through a reconnaissance field survey aided by a pre-event satellite image taken on 8 July 2013, available on Google Earth™, and by colour photographs taken in the field with a hand-held camera. The images were interpreted visually by an expert geomorphologist using the StereoMirror™ hardware technology combined with the ERDAS IMAGINE® and Leica Photogrammetry Suite (LPS) software. The eighth map, which we considered our reference showing the "ground truth", was obtained through a Real Time Kinematic Differential Global Positioning System (GPS) survey conducted by walking a GPS receiver along the landslide perimeter to capture geographic coordinates every about 5 m, with centimetre accuracy. The eight maps of the Assignano landslide were stored in a Geographic Information System (GIS), and compared adopting a pairwise approach. Results of the comparisons, quantified by the error index E, revealed that where the landslide signature was primarily photographical (in the landslide source and transport area) the best mapping results were obtained using the higher resolution images, and where the landslide signature was mainly morphometric (in the landslide deposit) the best results were obtained using the stereoscopic images. The ultra-resolution image proved very effective to map the landslide, with results comparable to those obtained using the stereoscopic satellite image. Conversely, the field-based reconnaissance mapping provided the poorest results, measured by large mapping errors, and confirmed the difficulty in preparing accurate landslide maps in the field. Albeit conducted on a single landslide, we maintain that our results are general, and provide useful information to decide on the optimal imagery for the production of event, seasonal and multi-temporal landslide inventory maps.

1 Introduction

Accurate detection of single landslides has different scopes, including landslide mapping (Di Maio and Vassallo, 2011; Manconi et al., 2014; Plank et al., 2016), landslide hazard analysis and risk assessment (Allasia et al., 2013), to support the installation of landslide monitoring systems (Tarchi et al., 2003; Teza et al., 2007; Monserrat and Crosetto, 2008; Giordan et al., 2013), and for landslide geotechnical characterization and modelling (Gokceoglu, 2005; Rosi et al., 2013). Mapping of single landslides can be executed using the same techniques and tools commonly used by geomorphologists to prepare landslide inventory maps i.e., through field surveys (Santangelo et al., 2010) or the heuristic visual interpretation of monoscopic or stereoscopic aerial or satellite images (Brardinoni et al., 2003; Fiorucci et al., 2011; Ardizzone et al., 2013), of LiDAR-derived images (Ardizzone et al., 2007; Van Den Eeckhaut et al., 2007; Haneberg et al., 2009; Giordan et al., 2013; Razak et al., 2013; Niculita et al., 2016, Petschko et al., 2016), or of ultra-resolution images acquired by Unmanned Aerial Vehicles (UAV, Niethammer et al., 2010, Giordan et al., 2015a, 2015b; Torrero et al., 2015, Turner et al., 2015). The heuristic visual mapping of landslide features is based on the systematic analysis of image photographic and morphological characteristics such as colour, tone, mottling, texture, shape, size, curvature (Pike, 1988). These photographic and morphological characteristics encompasses all the possible landslide features that can be used for the (visual) interpretation of the available imagery.

All these mapping techniques have inherent advantages and intrinsic limitations, which depend on the size and type of the landslides, and on the characteristics of the images, including their spatial and spectral resolutions (Fiorucci et al., 2011). As a result, landslide maps prepared exploiting one or more of the mentioned techniques are inevitably incomplete, and contain errors in terms of the position, size and shape of the mapped landslides (Guzzetti et al., 2000; Galli et al., 2008, Santangelo et al., 2015a).

Attempts have been made to evaluate the errors associated to different types of landslide inventory maps (Carrara et al., 1992; Ardizzone et al., 2002, 2007; Van Den Eeckhaut et al., 2007; Fiorucci et al., 2011; Santangelo et al., 2010; Mondini et al., 2013). Most of these attempts compare landslide maps prepared using aerial or satellite images to maps obtained through reconnaissance field mapping (Ardizzone et al., 2007; Fiorucci et al., 2011) or GPS surveys (Santangelo et al., 2010). Conversely, only a few authors have attempted to evaluate the influence of different types

75   of imagery on landslide detection and mapping (Carrara et al., 1992).

76   In this work, we evaluate how images of different types and characteristics influence event

77   landslide mapping. We do this by comparing eight maps of a single, rainfall-induced landslide near

78   the village of Assignano, Umbria, central Italy. Seven maps of the same landslide were obtained

79   using different techniques and images, including (i) a reconnaissance field survey, (ii) the

80   interpretation of ultra-resolution images taken by an optical camera on-board an UAV, and (iii) the

81   visual interpretation of Very High Resolution (VHR), monoscopic and stereoscopic, multispectral

82   images taken by the WordView-2 satellite. These maps were compared to an eighth map considered

83   to be the benchmark showing the "ground truth" i.e., the "true" position, shape and extent of the

84   Assignano landslide. Based on the results of the map comparison, we infer the ability of different

85   optical images, with different spectral and spatial characteristics, to portray the landslide features

86   that can be exploited for the visual detection and mapping of landslides. We maintain that the

87   results obtained in our test case are general, and should be considered for the optimal selection of

88   images for the detection and mapping event landslides.

2 The Assignano landslide

90   For our study, we selected the Assignano landslide, a slide-earthflow (Hutchinson, 1970) triggered

91   by intense rainfall in December 2013 in the northwest-facing slope of the Assignano village,

92   Umbria, central Italy (**Fig. 1**). The landslide develops in a crop area, where a layered sequence of

93   sand, silt and clay deposits crop out (Santangelo et al., 2015b). The slope failure is about 340 m

94   long, 40 m wide in the transportation area, and 60 m wide in the deposition area, and is

95   characterized by three distinct source areas, two located on the south-west side of the landslide and

96   third located on the north-east side of the landslide. The source and transportation area has an

97   overall length of about 230 m, and a width increasing from 10 to 40 m from the top of the source

98   area to the bottom of the transportation area. Elevation in the landslide ranges from 276 m along

99   the landslide crown, to 206 m at the lowest tip of the deposit. The source and transportation area is

100   bounded locally by sub-vertical, 2 to 4-m high escarpments. In the landslide, terrain slope averages

101   $11°$, and is steeper ($12°$) in the source and transportation area than in the deposition area ($9°$). The

102   landslide signature (Pike, 1988) is different in the different parts of the landslide. In the source and

103   transport area the signature is predominantly photographical (radiometric), whereas in the landslide

104   deposit it is mainly morphometric (topographic). The differences allow to separate the source and

105   transportation area from the deposition area.

3 Image acquisition

107   On 14 April 2014, we conducted an aerial survey of the Assignano landslide using a "X" shaped
108   frame octocopter with eight motors mounted on four arms (four sets of CW and CCW props) with
109   a payload capacity of around one kilogram, and a flight autonomy of about 20 minutes. The UAV
110   was equipped with a remotely controlled gimbal hosting a ©GoPro Hero 3 video camera and a
111   Canon EOS M camera. We controlled the flight of the UAV manually, relaying on the real-time
112   video stream provided by the ©GoPro. We kept the operational flight altitude of the UAV in the
113   range between 70 and 100 m above the ground. This allowed the Canon EOS M camera to capture
114   97 digital colour images of the landslide area with a ground resolution of about 2-4 cm, with the
115   single images having an overlap of about 70% and a side-lap of about 40%. For the accurate
116   geocoding of the images, we positioned 13 red-and-white, four-quadrants square targets,
117   20 cm $\times$ 20 cm in size, outside and inside the landslide. We obtained the geographical location
118   (latitude, longitude, elevation) of the 13 target centres using a Real Time Kinematic (RTK)
119   Differential Global Positioning System (DGPS), with a horizontal error of less than 3 cm. We
120   processed the 97 images using commercial, structure-from-motion software to obtain (i) a 3D point
121   cloud, (ii) a Digital Surface Model (DSM), and (iii) a digital, monoscopic, ultra-resolution (ground
122   sampling distance is 3×3 cm) ortho-rectified image in the visible spectral range, which we used
123   for the visual mapping of the Assignano landslide (**Table 1**).

124   To map the landslide, we also used a stereoscopic pair of VHR images taken on 14 April 2014 i.e.,
125   the same day of the UAV survey, by the WorldView-2 satellite that operates at an altitude of 496
126   km, and collects 46-cm panchromatic, and 1.84-m eight-band, multispectral (coastal blue, blue,
127   green, yellow, red, red edge, and near infrared-1, near-infrared-2) imagery at 11-bit dynamic range,
128   in the spectral range 0.400 – 1.040 μm. For the satellite imagery, the rational polynomial
129   coefficients (RPCs) are available, allowing for accurate photogrammetric processing of the images.
130   We used the RPCs to generate 3D models of the terrain from the stereoscopic image pair.
131   Exploiting the characteristics of the satellite image, we prepared four separate images for landslide
132   mapping, namely, (i) a monoscopic, "true colour" (TC) image, (ii) a monoscopic false-colour-
133   composite (FCC) image obtained from the composite near infrared, red and green (band 4,3,2), (iii)
134   a TC stereoscopic pair, and (iv) a FCC stereoscopic pair. We prepared separate maps of the

135   Assignano landslide through the visual interpretation of the four images (**Table 1**). Both satellite

136   and UAV images are free from deep shadows (**Fig. 2**).

137   To compare the images obtained by the UAV and the WorldView-2 satellite, we co-registered the

138   images, and we evaluated the co-registration on seven control points (**Fig. 3**), obtaining a Distance

139   Root Mean Square error, DRMS = 0.53 m, and a Circular Error Probability, $CEP_{50\%} = 0.42$ m,

140   which we consider adequate for landslide mapping, and for the map comparison.

4 Landslide mapping

142   We prepared eight maps of the Assignano landslide using different approaches, images and

143   datasets, including two maps prepared through field surveys, four maps prepared through the visual

144   interpretation of monoscopic and stereoscopic satellite images, and two maps prepared through the

145   visual interpretation of the orthorectified images taken by the UAV (**Table 1**).

146   The field mapping and the image interpretation were carried out by independent geomorphologists.

147   The two geomorphologists who carried out the field activities i.e., the reconnaissance field mapping

148   and the RTK-DGPS survey, were not involved in the visual interpretation of the satellite and the

149   UAV images. Equally, the geomorphologist who interpreted visually the satellite and the UAV

150   images did not take part in the field activities. Visual interpretation of the remotely-sensed images

151   was performed by a single geomorphologist to avoid problems related to different interpretation

152   skills by different interpreters (Carrara et al., 1992). We then compared the eight resulting maps of

153   the Assignano landslide adopting a pairwise approach to quantify and evaluate the mapping

154   differences.

155   The geomorphologist who interpreted visually the images was shown first the 1.84-m resolution,

156   monoscopic satellite image, next the 1.84-m resolution stereoscopic satellite pair, and lastly the 3-

157   cm resolution UAV images. The monoscopic and the stereoscopic satellite images were first shown

158   in TC and then in FCC. Lastly, the interpreter was shown the draped ultra-resolution UAV image.

159   Selection of the sequence of the images given to the geomorphologist for the expert driven visual

160   interpretation was based on the assumption that for landslide mapping (i) the ultra-resolution

161   monoscopic images provide more information than the 1.84-m monoscopic or stereoscopic images,

162   (ii) for equal spatial resolution images, stereoscopic images provide more information than

163   monoscopic images, and (iii) for equal image type (monoscopic, stereoscopic), the FCC images

164   provide more information than the TC images. To prevent biases related to a possible previous
165   knowledge of the landslide, the interpreter was not shown the results of the reconnaissance field
166   mapping.

4.1 Field mapping

168   Field mapping of the Assignano landslide consisted in two synergic activities, (i) a reconnaissance
169   field survey, and (ii) a RTK DGPS aided survey. First, the reconnaissance field survey was
170   conducted by two geomorphologists (FF and MR) who observed the landslide and took
171   photographs of the slope failure from multiple viewpoints, close to and far from the landslide. The
172   geomorphologists draw in the field a preliminary map of the landslide exploiting the most recent
173   satellite image available at the time in Google Earth™, which was taken on 8 July 2013 i.e. (**Fig.**
174   **4**), before the landslide occurred. The reconnaissance field mapping was then refined in the
175   laboratory using the ground photographs taken in the field. We refer to this reconnaissance
176   representation of the Assignano landslide as "Map B".

177   Next, the same two geomorphologists (FF and MR) conducted an RTK DGPS aided survey
178   walking a Leica Geosystems GPS 1200 receiver along the landslide boundary, capturing 3D
179   geographic coordinates every about 5 m, in 3D distance. For the purpose, we used the SmartNet
180   ItalPoS real-time network service to transmit the correction signal from the GPS base station to the
181   GPS roving station. The estimated accuracy obtained for each survey point measured along the
182   landslide boundary was 2 to 5 cm, measured by the root mean square error (RMSE), on the ETRF-
183   2000 reference system. We refer to the cartographic representation of the Assignano landslide
184   produced by the RTK DGPS survey as "Map A". We consider this map as the "ground truth", and
185   we use it as a benchmark against which to compare the other maps. We acknowledge that mapping
186   a landslide by walking a GPS receiver around its boundary is an error prone operation e.g., because
187   in places the landslide boundary is not sharp, or clearly visible from the ground (Santangelo et al.,
188   2010). However, we maintain this is the most reasonable working assumption, and that the
189   geometrical information obtained by walking a GPS receiver along the landslide boundary was
190   superior to the information obtained through the reconnaissance field mapping (Map B)
191   (Santangelo et al., 2010).

4.2 Mapping through image interpretation

193   A trained geomorphologist (MS) used the three monoscopic images (i.e., the TC and FCC

194   monoscopic satellite images, and the monoscopic ultra-resolution UAV image) to perform a
195   heuristic, visual mapping of the Assignano landslide. For this purpose, the interpreter considered
196   the photographic (colour, tone, mottling, texture) and geometrical (shape, size, curvature, pattern
197   of individual terrain features, or sets of features) characteristics of the images (Antonini et al.,
198   1999). In this way, the geomorphologist prepared (i) "Map C" interpreting visually the
199   monoscopic, TC satellite image, (ii) "Map D" interpreting visually the monoscopic, FFC satellite
200   image, and (iii) "Map G" interpreting visually the monoscopic, TC UAV image (**Table 1**).

201   Next, the interpreter used the two stereoscopic satellite images (i.e., the TC and FCC images) to
202   prepare "Map E" and "Map F" (**Table 1**). In the stereoscopic images, the photographic and
203   morphological information is combined, favouring the recognition of the landslide features through
204   the joint analysis of photographic (colour, tone, mottling, texture), geometrical (shape, size, pattern
205   of features), and morphological terrain features (curvature, convexity, concavity). To analyse
206   visually the stereoscopic satellite images, the interpreter used the StereoMirror™ hardware
207   technology, combined with the ERDAS IMAGINE® and Leica Photogrammetry Suite (LPS)
208   software. To map the landslide features in real-world, 3D geographical coordinates, the interpreter
209   used a 3D floating cursor (Fiorucci et al., 2015).

210   To interpret the ultra-resolution UAV image, the interpreter overlaid ("draped") the image on
211   Google Earth™. For the purpose, we first treated the UAV image with gdal2tiles.py software to
212   obtain a set of image tiles compatible with the Google Earth™ terrain visualization platform. To
213   interpret visually the ultra-resolution UAV image, the interpreter overlaid ("draped") the image on
214   Google Earth™. For the purpose, we first treated the UAV image with the gdal2tiles.py software
215   to obtain a set of image tiles compatible with Google Earth™ terrain visualization platform. To the
216   best of our knowledge, the platform is the only free, 2.5D image visualisation environment that
217   allows the editing of vector (i.e., point, line, polygon) information. Other commercial (e.g.,
218   ArcScene) and open source (e.g., ParaView, GRASS GIS), 2.5D visualization tools do not provide
219   editing capabilities. Google Earth™ is a user-friendly solution for mapping single landslides, and
220   for preparing landslide event inventories for limited areas, with the possibility for the user to
221   visualize a landscape from virtually any viewpoint, facilitating landslide mapping. We refer to the
222   representation of the Assignano landslide obtained through the visual interpretation of the ultra-
223   resolution UAV image as "Map H".

224　For the visual interpretation of the satellite and the UAV images, the interpreter adopted a

225　visualization scale in the range from 1:1000 to 1:6000, depending on the image spatial resolution

226　(**Table 1**). The scale of observation was selected to obtain the best readability of each landslide

227　feature and the surroundings, which is a common practice in image visual analysis for landslide

228　mapping (Fiorucci et al., 2011). Hence, even if the maps were produced at slightly different

229　observation scales, the differences arising from the comparison are due to actual features (i.e., the

230　image resolution and radiometry), and not to the different observation scales.

5 Results

231

232　Using the described mapping methods, and the available satellite and UAV images (**Table 1**), we

233　prepared eight separate and independent cartographic representations of the Assignano landslide,

234　shown in **Fig. 5** as Map A to Map H.

235　Considering the entire landslide, visual inspection of **Fig. 5** reveals that the maps most similar to

236　the benchmark (Map A) are Map E, prepared examining the true colour (TC) stereoscopic satellite

237　image, and Map F, prepared examining the false colour composite (FCC) stereoscopic satellite

238　image. Conversely, the largest differences were observed for the landslide maps obtained through

239　the reconnaissance field survey (Map B), and the visual interpretation of the monoscopic satellite

240　images (Map C and Map D). Considering only the source and transportation areas (dark colours in

241　**Fig. 5**), interpretation of the UAV ultra-resolution images resulted in the landslide maps most

242　similar (Map G and Map H) to the benchmark (Map A). It is worth noticing the systematic lack in

243　the mapping of one of the two secondary landslide source areas located in the SW side of the

244　landslide, which was recognized only from the visual inspection of the ultra-resolution

245　orthorectified images taken by the UAV. In the field, this source area was characterized by small

246　cracks along the escarpment and a limited disruption of the meadow, making it particularly difficult

247　to detect and map. We argue that only the ultra-resolution images allowed for the detection of the

248　cracks. Considering only the landslide deposit (light colours in **Fig. 5**), the landslide mapping that

249　was more similar to the benchmark (Map A) was obtained interpreting the TC, stereoscopic

250　satellite images (Map E). We also note that in most of the maps the landslide deposit was mapped

251　larger (Map G, Map H) or much larger (Map B, Map C and Map D) than the benchmark (Map A).

252　**Table 2** lists geometric measures of the mapped landslides, including the planimetric measurement

253   of length, width and area (i) of the entire landslide, (ii) of the landslide source and transportation

254   area (dark colours in **Fig. 5**), and (iii) of the landslide deposit (light colours in **Fig. 5**). The length

255   and width measurements were obtained in a GIS as the length and the width of the minimum

256   oriented rectangle encompassing (i) the entire landslide, (ii) the landslide source and transportation

257   area, and (iii) the landslide deposit. Our benchmark (Map A) has a total area $A_L = 1.1 \times 10^4$ m^2, and

258   is $L_{LS} = 362$ m long and $W_{LS} = 71$ m wide. Amongst the other seven maps (Map B to Map H in

259   **Fig. 5**), the largest landslide is shown in Map B, obtained through the reconnaissance field

260   mapping, and has $A_L = 1.91 \times 10^4$ m^2, 71.1% larger than the benchmark. Conversely, the smallest

261   landslide is shown in Map F, with $A_L = 1.1 \times 10^4$ m^2, 4.6% smaller than the benchmark. The longest

262   and largest landslide is found in Map C, with $L_{LS} = 405$ m (11% longer than the benchmark) and

263    $W_{LS} = 113$ m (60% wider than the benchmark).

264   Considering the source and transportation area, in Map A (the benchmark) $A_{LS} = 5.4 \times 10^3$ m^2,

265    $L_{LS} = 228$ m, and $W_{LS} = 52$ m. The largest representation of the source and transportation area is

266   found in Map B (reconnaissance field mapping) with $A_{LS} = 7.4 \times 10^3$ m^2, 36.9% larger than the

267   benchmark, and the smallest source and transportation area is found in Map G, with

268    $A_{LS} = 5.2 \times 10^3$ m^2, 3.6% smaller than the benchmark. The longest source and transportation area is

269   found in Map F, with $L_{LS} = 239$ m, 5% longer than the benchmark, and the shortest source and

270   transportation area is shown in Map C, with $L_{LS} = 206$ m, 9.7% shorter than the benchmark. The

271   largest source and transportation area is shown in Map B, $W_{LS} = 60$ m, 15.7% wider than Map A,

272   and the narrowest source and transportation area is in Map C, $L_{LS} = 44$ m, 15.3% narrower than the

273   benchmark. Considering instead only the landslide deposit, our benchmark (Map A) has

274    $A_{LD} = 5.7 \times 10^3$ m^2, $L_{LS} = 153$ m, and $W_{LS} = 61$ m. The largest deposit is shown in Map B

275   (reconnaissance field mapping) and has $A_{LD} = 1.2 \times 10^4$ m^2, 103.4% larger than the benchmark,

276   whereas the smallest landslide deposit is shown in Map F, with $A_{LD} = 4.6 \times 10^3$ m^2, 19.8% smaller

277   than the benchmark. Analysis of the length and width of the landslide deposit reveals that Map C

278   shows the longest deposit, $L_{LS} = 206$ m, 35% longer than the benchmark, and Map H shows the

279   shortest deposit, $L_{LS} = 122$ m, 20.2% shorter than the benchmark. Similarly, the largest landslide

280   deposit is shown in Map C, $W_{LS} = 112$ m, 82.8% wider than the benchmark, and the narrowest

281   landslide deposit is portrayed in Map E, $W_{LS} = 56$ m, 8.2% less than the benchmark.

282   To compare quantitatively the different landslide maps, we use the error index *E* proposed by

283   Carrara et al. (1992), adopting the pairwise comparison approach proposed by Santangelo et al.

284   (2015a). The index provides an estimate of the discrepancy (or similarity) between corresponding

285   polygons in two maps, and is defined as:

$$E = \frac{(A \cup B) - (A \cap B)}{(A \cup B)}; \ 0 \leq E \leq 1, \tag{1}$$

286   where, A and B are the areas of two corresponding polygons in the compared maps, and ∪ and ∩

287   are the geographical (geometric) union and intersection of the two polygons, respectively. E spans

288   the range from 0 (perfect matching) to 1 (complete mismatch).

289   We compared the eight maps of the Assignano landslide (**Fig. 5**) adopting a pairwise approach,

290   and considering first only the landslide source and transportation area, next only the landslide

291   deposit, and lastly the entire landslide. **Fig. 6** summarizes the 84 values of the error index E, 28 for

292   the landslide source and transportation area (**Fig. 6 I**), 28 for the landslide deposit (**Fig. 6 II**), and

293   28 for the entire landslide (**Fig. 6 III**). On average, the source and transportation area exhibits

294   values of the error index smaller than the values found in the landslide deposit. This indicates that

295   in the source and transportation area the landslide maps are more similar than in the landslide

296   deposit. Inspection of **Fig. 6 I**, reveals a decrease of the error index in the source and transportation

297   area for the maps obtained interpreting the available images (from Map C to Map H), compared to

298   our benchmark obtained through the RTK DGPS survey ($0.15 \leq E \leq 0.38$), with Map G obtained

299   interpreting the TC, monoscopic, ultra-resolution UAV image. In the landslide deposit (**Fig. 6 II**),

300   the minimum difference ($E = 0.21$) was found comparing the benchmark to Map E, obtained

301   through the interpretation of the stereoscopic TC satellite image, and the largest difference

302   ($E = 0.52$) was found comparing the benchmark to Map C, prepared interpreting the TC,

303   monoscopic, satellite image.

304   Comparison of the maps obtained through the interpretation of the monoscopic images (Map C and

305   Map D), and the maps obtained through the interpretation of stereoscopic (Map E and Map F) or

306   ultra-resolution images (Map G and Map H), reveals high values of the error index, which is

307   slightly worse in the landslide deposit. This is evident in the source and transportation area

308   ($0.31 \leq E \leq 0.44$) (**Fig. 6 I**), and in the landslide deposit ($0.43 \leq E \leq 0.63$) (**Fig. 6 II**). Map C and

309   Map D are very similar, with a mapping error $E = 0.17$. Maps obtained through the interpretation

310   of stereoscopic satellite images (Map E and Map F, prepared using TC and FCC images,

311 respectively), and maps prepared by interpreting the UAV images (Map G and Map H), exhibit a

312 generally low value of E. In particular, $0.14 \leq E \leq 0.26$ in the landslide source and transportation

313 area, and $0.15 \leq E \leq 0.38$ in the landslide deposit. The reconnaissance field mapping (Map B)

314 exhibited the largest differences compared to all the other maps ($0.63 \leq E \leq 0.45$) in the landslide

315 source and transportation area, and $0.44 \leq E \leq 0.73$ in the landslide deposit. The large values of E

316 in the landslide deposit is probably due to lack of visibility of part of the landslide toe in the field.

6 Discussion

318 We discuss the ability of the different images used to detect and map the Assignano landslide (**Fig.**

319 **1**) to resolve the landslide photographical and morphological signatures, considering separately the

320 image spatial and spectral resolutions, and the image type i.e., monoscopic, stereoscopic, or

321 pseudo-stereoscopic. We treat each of the three factors separately, keeping the other two factors

322 constant. To evaluate the influence of the image spatial resolution on landslide mapping, we

323 compare to our benchmark (Map A) two true-colour (TC) monoscopic maps (Map C and Map G),

324 and two TC stereoscopic maps (Map E and Map H). Next, to evaluate the influence of the image

325 spectral resolution on the landslide mapping, we compare to the benchmark (Map A) the TC and

326 the false-colour-composite (FCC) monoscopic maps (Map C and Map D), and the corresponding

327 TC and FCC stereoscopic maps (Map E and Map F). Lastly, to assess the influence of the type of

328 image (i.e., monoscopic, stereoscopic, pseudo-stereoscopic) on the landslide mapping, we compare

329 to the benchmark (Map A) the monoscopic (Map C) and the stereoscopic (Map E) TC maps

330 (**Fig. 7A**), the two FCC maps (Map D and Map F) (**Fig. 7B**), and the maps obtained interpreting

331 the ultra-resolution images captured by the UAV (Map G and Map H). **Fig. 6** summarizes the

332 mapping errors E obtained by the pairwise comparisons of the eight landslide maps shown in **Fig. 5**.

333 We first evaluate the role of the image spatial resolution in the production of the different maps of

334 the Assignano landslide. Inspection of **Fig. 6 I** reveals that the maps of the landslide source and

335 transportation area obtained from images characterized by the highest spatial resolution (i.e.,

336 Map G and Map H) exhibits the smallest errors ($E \leq 0.16$), when compared to the benchmark

337 (Map A). The mapping error obtained for Map C (TC, monoscopic, $E = 0.38$) is 2.5 times larger

338 than the error obtained using the ultra-resolution orhtorectified images taken by the UAV (Map G,

339 $E = 0.15$, and Map H, $E = 0.16$), whereas the error obtained from Map E (TC, stereoscopic,

340 $E = 0.23$) is smaller, and about 1.5 times larger than the error obtained for Map H (TC, pseudo-

stereoscopic, $E = 0.16$). In the landslide deposit (**Fig. 6 II**), the map obtained exploiting the monoscopic, TC satellite image (Map C) exhibits an error $E = 0.52$, 1.7 times larger than the error obtained using Map G (TC, monoscopic UAV, $E = 0.30$). Conversely, the error is smaller in the map obtained from the 2-m spatial resolution, stereoscopic TC satellite image (Map E, $E = 0.21$) than from the 3-cm spatial resolution, pseudo-stereoscopic image taken by the UAV (Map H, $E = 0.30$). Collectively, the pairwise comparisons highlights an improvement of the quality of the mapping of the landslide features that exhibits a distinct photographical signature, most visible in the source and transportation area of the Assignano landslide, with an increase of the image spatial resolution (**Fig. 6**). Use of the ultra-resolution image captured by the UAV did not result in an improvement of the mapping in the deposition area of the Assignano landslide, where the landslide exhibits a distinct morphological signature. We further observe that most of the landslide parts that were not identified in the maps prepared using the satellite image are covered by vegetation, locally bounded by small and thin cracks with an average width smaller than the size of the 2×2 m pixel. In the satellite image, the cracks are located in pixels containing a mix of vegetation and bare soil, making it difficult for the interpreter to recognize the cracks.

Next, we evaluate the effectiveness of the image spectral resolution, and for the purpose we examine the mapping errors of Maps C and Map E (TC), and of Map D and Map F (FCC). The mapping of the source and transportation area prepared using the false-colour-composite (FCC) images (Map D and Map F) resulted in smaller errors than the mapping prepared using the corresponding true-colour (TC) images (Map C and Map E), for both monoscopic and stereoscopic images (**Fig. 6 I**). In the source and transportation area, the false-colour-composite emphasized the presence or absence of the vegetation, and contributed locally to highlight the typical photographical signature of the landslide, which helped the photo-interpreter to detect and map the slope failure. Conversely, in the landslide deposition area (**Fig. 6 II**) use of the FCC images did not result in a systematic reduction of the mapping error, when compared to the TC images. We conclude that use of the additional information contributed by the Near Infrared (NIR) band in the 1.84-m resolution satellite image did not improve the quality of the mapping. On the other hand, the contribution of the NIR in the 3-cm UAV image remains unknown.

Next, we evaluate the influence of the image type (i.e., monoscopic, stereoscopic, pseudo-stereoscopic) on the mapping error by comparing (i) the TC images (Map C and Map E), (ii) the

371   FCC images (Map D and Map F), and (iii) the ultra-resolution UAV image (Map G and Map H).

372   Comparison of the TC, monoscopic (Map C) and stereoscopic (Map E) images revealed a mapping

373   error for the entire landslide $E = 0.48$, with the mismatch larger in the deposition area ($E = 0.59$)

374   than in the source and transpiration area ($E = 0.45$) (**Fig. 6**). A similar result was obtained

375   comparing the FCC, monoscopic (Map D) and stereoscopic (Map F) images, with a mapping error

376   for the entire landslide $E = 0.44$, and again the mismatch is larger in the deposition area ($E = 0.60$)

377   than in the source and transpiration area ($E = 0.36$). In the deposition area, where the morphological

378   signature of the Assignano landslide is strongest, the mapping error obtained comparing our

379   benchmark (Map A) to the landslide maps prepared using the monoscopic images (Map C and

380   Map D) is 2 times larger than the error observed for the maps prepared using the corresponding

381   stereoscopic images (Map E and Map F). The differences are smaller in the source and

382   transportation area, where the morphological signature of the landslide is less distinct. Direct

383   comparison of Map E (TC, stereoscopic) and Map F (FCC, stereoscopic) for the entire landslide

384   reveals a very small mapping error ($E = 0.15$), indicating the similarity of the two maps, which

385   were also very similar to the benchmark (Map A), $E \leq 0.20$.

386   Comparison for the entire landslide of the maps prepared using the ultra-resolution images captured

387   by the UAV (Map G and Map H) exhibits the smallest error of all the pairwise comparisons

388   ($E = 0.08$) (**Fig. 6 III**), indicating the large degree of matching between the two maps. The degree

389   of matching is only marginally smaller in the source and transportation area, and in the deposition

390   area ($E = 0.15$). When compared to our benchmark (Map A), Map G and Map H exhibit a small

391   error ($E = 0.19$) for the entire landslide, which is larger in the deposition area ($E \leq 0.30$) and slightly

392   smaller in the source and transport area ($E \leq 0.15$). Interestingly, the mismatch with Map A (the

393   benchmark) is lower for the monoscopic (Map G) than for the pseudo-stereoscopic (Map H) map.

394   The finding highlights the lack of an advantage in using a pseudo-stereoscopic (2.5D) image for

395   mapping the Assignano landslide. We attribute this result to the low resolution of the (pre-event)

396   DEM used to drape the ultra-resolution image for visualization purposes, which did not add any

397   significant morphological information to the expert visual interpretation.

398   Joint analysis of **Fig. 5B** and **Fig. 6** reveals that, when compared to our benchmark (Map A), the

399   reconnaissance field mapping (Map B) exhibited the largest mapping error of all the performed

400   pairwise comparisons, with $E = 0.45$ in the source and transportation area, $E = 0.67$ in the landslide

401   deposit, and $E = 0.55$ for the entire landslide. We note than an error of $E = 0.50$ indicates that 50%

402   of the landslide area in one map (Map B, in this case) does not overlay with the other map (Map A,

403   the benchmark, in this case). Our results are similar to the results of tests performed to compare

404   field-based landslide maps against GPS-based surveys of single landslides (Santangelo et al.,

405   2010), the visual interpretation of very-high resolution stereoscopic satellite images (Ardizzone

406   et al., 2013), or the semi-automatic processing of monoscopic satellite images (Mondini et al.,

407   2013), and confirm the inherent difficulty in preparing accurate landslide maps in the field, unless

408   the mapping is supported by a GPS survey or a similar technology.

409   Our experiment showed that the mapping of the Assignano landslide obtained exploiting the ultra-

410   resolution images captured by the UAV (Map G and Map H) was comparable to the maps obtained

411   using the high resolution stereoscopic satellite image (Map E and Map F), and to the ground-based

412   RTK DGPS survey (Map A, the benchmark). We conclude that ultra-resolution images captured

413   by an UAV and the stereoscopic satellite images are well suited to map event landslides, at least in

414   physiographical settings similar to the one of our study area, and for landslides similar to the

415   Assignano landslide (**Fig. 1**).

416   For event landslide mapping, selection between ultra-resolution pseudo-stereoscopic UAV images

417   and very-high resolution stereoscopic satellite images depends on (i) the extent of the investigated

418   area, (ii) the available resources, including time and budget, and (iii) the accessibility to the study

419   area. The selection is largely independent from the landslide signature, at least for landslides similar

420   to the Assignano landslide. From an operational perspective, modern multi-rotor UAVs allow for

421   the acquisition of ultra-resolution images over small areas in a limited time, and at very low costs.

422   UAV-based surveys are flexible in their acquisition planning, and partly independent from the local

423   lighting conditions, including the cloud cover. As a drawback, UAVs are strongly (and negatively)

424   affected by wind speed and weather conditions, they allow for a limited flight time (currently

425   approximately 20 minutes in optimal conditions), which is reduced in bad weather conditions and

426   in cold environments, and typically have limited data storage capacity. Further, it must be possible

427   for the pilot to be at the same time near to the area to be surveyed and to maintain a safe distance

428   from the UAV, a condition that may be difficult to attain in remote or in mountain areas.

429   Collectively, the intrinsic advantages and limitations of modern UAVs make the technology

430   potentially well suited for the acquisition of ultra-resolution images for event, seasonal, and multi-

431 temporal mapping of single landslides, of multiple landslides in a single slope, or in a relatively

432 small area (a few hectares). The use of UAV images was recently proposed by Turner et al. (2015)

433 for determining the landslide dynamics, exploiting time series of images that can be constructed

434 using UAVs. The result is achievable thanks to centimetre co-registration accuracy of the UAV

435 images. Use of UAVs becomes impracticable with the increasing extent of the study area, largely

436 due to (i) the operational difficulty of flying UAVs over large areas (more than a few square

437 kilometres), and (ii) the acquisition and image processing time and associated cost, which increase

438 rapidly with the size of the study area (**Table 3**). On the other hand, very-high resolution,

439 stereoscopic satellite images have also advantages and limitations for the production of event,

440 seasonal and multi-temporal landslide inventory maps (Guzzetti et al., 2012). The main advantage

441 of the satellite images is that they cover large or very areas (tens to hundreds of square kilometres)

442 in a single frame with a sub-metre resolution well suited for landslide mapping through the expert

443 visual interpretation of the images (Ardizzone et al., 2013). On the other hand, limitations remain

444 due to distortions caused by different off-nadir angles in successive scenes, and to difficulties – in

445 places severe – to obtaining suitable (e.g., cloud-free) images at the required time intervals. This is

446 particularly problematic for the production of seasonal and multi-temporal landslide maps.

447 Information on the photographic or morphological signature of the typical, or most abundant,

448 landslides in an area, is important to selecting the optimal characteristics of the images best suited

449 for the production of an event, seasonal or multi-temporal landslide inventory map. Use of images

450 of non-optimal characteristics for a typical landslide signature in an area may condition the quality

451 (i.e., completeness, positional and thematic accuracy) of the landslide inventory. Where possible,

452 we recommend that the acquisition of images used for the production of event, seasonal or multi-

453 temporal landslide inventory maps is planned considering the typical landslide signature, in

454 addition to the purpose (event inventory, planning of monitoring systems), scale of the mapping

455 (i.e. regional or slope scale), and the size and complexity of the study area (**Table 3**).

7 Concluding remarks

457 We executed an experiment aimed at determining and measuring the effects of the image

458 characteristics on event landslide mapping. In the experiment, we compared landslide maps

459 obtained (i) through the expert visual interpretation of an ultra-resolution image taken by an UAV

460 with a ground resolution of 3×3 cm, and monoscopic and stereoscopic true-colour and false-

461   colour-composite (1.84 × 1.84 m) images taken by the WorldView-2 satellite, (ii) a reconnaissance

462   field survey of the landslide, and (iii) an accurate survey of the landslide obtained by walking a

463   GPS receiver along the landslide boundary. We conducted the experiment on a the Assignano

464   landslide (**Fig. 1**) triggered by intense rainfall in December 2013 in the northwest-facing slope of

465   the Assignano village, Umbria, central Italy. The landslide exhibited a predominant photographical

466   (radiometric) signature in the source and transport area, and a more distinct morphological

467   (topographic) signature in the deposition area. The results of our mapping experiment allow for the

468   following conclusions.

469   First, in the landslide source and transport area, where the signature of the slope failure was

470   primarily photographical (radiometric), mapping errors (Carrara et al., 1992; Santangelo et al.,

471   2015a) decreased with the increase of the spatial resolution of the images used for the expert visual

472   detection and mapping of the landslide. In the same area, the image photographic (radiometric)

473   characteristics (true-colour, false-colour-composite) and the image type (monoscopic,

474   stereoscopic) played a minor role in augmenting the quality of the landslide map. Conversely, in

475   the deposition area, where the signature of the landslide was primarily morphological

476   (topographical), mapping errors decreased using stereoscopic satellite images that allowed

477   detecting topographic features distinctive of the landslide.

478   FCC and TC in the stereoscopic satellite images give similar values of the error. This indicates that

479   the spectral resolution of the images does not provide useful information to recognize and map the

480   landslide morphological features. On the other hand, the high spatial resolution provided by the

481   UAV images reduces the error, when compared to the monoscopic satellite imagery. However, the

482   error obtained using the UAV images remains higher than that obtained using stereoscopic satellite

483   images, despite the latter having a pixel one order of magnitude larger than the UAV images. We

484   conclude that the increase in the spatial resolution improves the ability to map morphological

485   features when using monoscopic images.

486   Second, use of the stereoscopic satellite images resulted in more accurate landslide maps (lower

487   error index E) than the corresponding monoscopic images in the landslide deposition area, where

488   the signature of the landslide was primarily morphometric (topographic). This was expected, as the

489   stereoscopic vision allowed to better capture the 3D terrain features typical of a landslide (Pike,

490   1988), including curvature, convexity and concavity. Conversely, visual examination of the false-

491 colour-composite images resulted in more accurate maps than the corresponding true-colour
492 images in the landslide source and transport area, where the signature of the landslide was primarily
493 photographic (radiometric). This was also expected (Guzzetti et al., 2012). Expert visual
494 interpretation of pseudo-stereoscopic ultra-resolution image failed to provide better results than the
495 corresponding monoscopic ultra-resolution image, most probably because the DEM used to drape
496 (overlay) the image on the terrain information was of low resolution.

497 Third, the ultra-resolution (3×3 cm) image captured by the photographic camera flown on-board
498 the Unmanned Aerial Vehicle (UAV) proved to be very effective to detect and map the landslide.
499 The expert visual interpretation of the monoscopic ultra-resolution image provided mapping results
500 comparable to those obtained using the about 2-m resolution, stereoscopic satellite image.

501 Fourth, a comparative analysis of the technological constrains and the costs of acquisition and
502 processing of ultra-resolution imagery taken by UAV, and of high, or very-high resolution imagery
503 taken by optical satellites, revealed that the ultra-resolution images are well suited to map single
504 event landslides, clusters of landslides in a single slope, or a few landslides in nearby slopes in a
505 small area (up to few square kilometres, Giordan et al., 2017) , and prove unsuited to cover large
506 and very large areas where the stereoscopic satellite images provide the most effective option
507 (Boccardo et al., 2015).

508 Fifth, our field-based reconnaissance mapping (Map B) provided the least accurate mapping
509 results, measured by the largest mapping error ($E = 0.55$ for the entire landslide) when compared
510 to the benchmark map (**Fig. 6**). Our results confirm the inherent difficulty in preparing accurate
511 landslide maps in the field through a reconnaissance mapping (Santangelo et al., 2010).

512 Although we conducted our study on a single landslide (**Fig. 1**), we maintain that the findings are
513 general, and can be useful to decide on the optimal imagery and technique to be used when planning
514 the production of a landslide inventory map. We emphasize that the technique and imagery used
515 to prepare landslide inventory maps should be selected depending on multiple factors, including (i)
516 the typical or predominant landslide signature (photographic or morphological), (ii) the scale and
517 size of the study area (a single slope, a small catchment, a large region), and (iii) the scope of the
518 mapping (event, seasonal, multi-temporal, Guzzetti et al., 2012).

8 Acknwoledgements

9 References

Allasia, P., Manconi, A., Giordan, D., Baldo, M., and Lollino, G.: ADVICE: a new approach for near-real-time monitoring of surface displacements in landslide hazard scenarios. Sensors, 13, 7, 8285-8302, https://doi.org/10.3390/s130708285, 2013.

Antonini, G., Ardizzone, F., Cardinali, M., Galli, M., Guzzetti, F. and Reichenbach, P.: Surface deposits and landslide inventory map of the area affected by the 1997 Umbria-Marche earthquakes, Boll. Soc. Geol. It., 121, 843-853, 2002.

Ardizzone, F., Cardinali, M., Carrara, A., Guzzetti, F., and Reichenbach, P.: Impact of mapping errors on the reliability of landslide hazard maps, Nat. Hazards Earth Syst. Sci., 2, 3-14, https://doi.org/10.5194/nhess-2-3-2002, 2002.

Ardizzone, F., Cardinali, M., Galli, M., Guzzetti, F., and Reichenbach, P.: Identification and mapping of recent rainfall-induced landslides using elevation data collected by airborne Lidar, Nat. Hazards Earth Syst. Sci., 7, 637-650, https://doi.org/10.5194/nhess-7-637-2007, 2007.

Ardizzone, F., Fiorucci, F., Santangelo, M., Cardinali, M., Mondini, A.C., Rossi, M., Reichenbach, P., and Guzzetti, F.: Very-high resolution stereoscopic satellite images for landslide mapping. C. Margottini, P. Canuti, K. Sassa (Eds.), Landslide Science and Practice, Landslide Inventory and Susceptibility and Hazard Zoning, 1, Springer, Heidelberg, Berlin, New York, 95–101, https://doi.org/10.1007/978-3-642-31325-7_12, 2013.

Boccardo, P., Chiabrando, F., Dutto, F., Tonolo, F.G., Lingua, A.: UAV deployment exercise for mapping purposes: evaluation of emergency response applications. Sensors, 15, 15717-15737, 2015, https://doi.org/10.3390/s150715717.

Brardinoni, F., Slaymaker, O., and Hassan, M.A.: Landslides inventory in a rugged forested watershed: a comparison between air-photo and field survey data, Geomorphology, 54, 179-196, https://doi.org/10.1016/S0169-555X(02)00355-0, 2003.

Carrara, A., Cardinali, M., and Guzzetti, F.: Uncertainty in assessing landslide hazard and risk, ITC Journal, 2, 172-183, 1992.

Di Maio, C., and Vassallo, R.: Geotechnical characterization of a landslide in a Blue Clay slope, Landslides, 8, 17-32, https://doi.org/10.1007/s10346-010-0218-8, 2011.

Fiorucci, F., Cardinali, M., Carlà, R., Rossi, M., Mondini, A. C., Santurri, L., Ardizzone, F., and Guzzetti, F.: Seasonal landslides mapping and estimation of landslide mobilization rates using aerial and satellite images, Geomorphology, 129, 59-70, https://doi.org/10.1016/j.geomorph.2011.01.013, 2011.

Fiorucci, F.; Ardizzone, F.; Rossi, M.; Torri, D.: The Use of Stereoscopic Satellite Images to Map Rills and Ephemeral Gullies. Remote Sens., 7, 14151-14178, https://doi.org/10.3390/rs71014151, 2015.

Galli, M., Ardizzone, F., Cardinali, M., Guzzetti, F., and Reichenbach, P.: Comparing landslide inventory maps, Geomorphology, 94, 268–289, https://doi.org/10.1016/j.geomorph.2006.09.023, 2008.

Giordan, D., Allasia, P., Manconi, A., Baldo, M., Santangelo, M., Cardinali, M., Corazza, A., Albanese, V., Lollino, G., and Guzzetti, F.: Morphological and kinematic evolution of a large earthflow: The

Montaguto landslide, southern Italy, Geomorphology, 187, 61-79, https://doi.org/10.1016/j.geomorph.2012.12.035, 2013.

Giordan, D., Manconi, A., Allasia, P., and Bertolo, D.: Brief Communication: On the rapid and efficient monitoring results dissemination in landslide emergency scenarios: the Mont de La Saxe case study, Nat. Hazards Earth Syst. Sci., 15, 2009-2017, https://doi.org/10.5194/nhess-15-2009-2015, 2015a.

Giordan, D., Manconi, A., Facello, A., Baldo, M., dell'Anese, F., Allasia, P., and Dutto, F.: Brief Communication: The use of an unmanned aerial vehicle in a rockfall emergency scenario, Nat. Hazards Earth Syst. Sci., 15, 163-169, https://doi.org/10.5194/nhess-15-163-2015, 2015b.

Giordan, D., Manconi, A., Remondino, F., Nex, F.: Use of unmanned aerial vehicles in monitoring application and management of natural hazards, Geomatics, natural hazards and risk, 8(1), 1-4, 2017.

Gokceoglu, C., Sonmez, H., Nefeslioglu, H. A., Duman, T. Y., Can, T.: The 17 March 2005 Kuzulu landslide (Sivas, Turkey) and landslide-susceptibility Map of its near vicinity. Engineering Geology, 81, 1, 65-83, https://doi.org/10.1016/j.enggeo.2005.07.011, 2005.

Guzzetti, F., Cardinali, M., Reichenbach, P., Cipolla, F., Sebastini, C., Galli, M., and Salvati, P.: Landslides triggered by the 23 November 2000 rainfall event in the Imperia Province, Western Liguria, Italy, Eng. Geol., 73, 229–245, https://doi.org/10.1016/j.enggeo.2004.01.006, 2000.

Guzzetti, F., Mondini, A. C., Cardinali, M., Fiorucci, F., Santangelo, M., and Chang, K.-T.: Landslide inventory maps: new tools for and old problem, Earth-Sci. Rev., 112, 42-66, https://doi.org/10.1016/j.earscirev.2012.02.001, 2012.

Haneberg, W. C., Cole, W. F., and Kasali, G.: High-resolution lidarbased landslide hazard mapping and modeling, UCSF Parnassus Campus; San Francisco, USA, B. Eng. Geol. Environ., 68, 263-276, https://doi.org/10.1007/s10064-009-0204-3, 2009.

Hutchinson, J. N.: A coastal mudflow on the London clay cliffs at Beltinge, North Kent, Geotechnique, 24, 412–438, 1970.

Manconi, A., Casu, F., Ardizzone, F., Bonano, M., Cardinali, M., De Luca, C., Gueguen, E., Marchesini, Parise, M., Vennari C., Lanari, R., Lanari, R.: Brief Communication: Rapid mapping of landslide events: the 3 December 2013 Montescaglioso landslide, Italy. Natural Hazards and Earth System Sciences, 14, 7, 1835, https://doi.org/10.5194/nhess-14-1835-2014, 2014.

Mondini, A. C., Marchesini, I., Rossi, M., Chang, K.-T., Pasquariello, G., and Guzzetti, F.: Bayesian framework for mapping and classifying shallow landslides exploiting remote sensing and topographic data, Geomorphology, 201, 135-147, https://doi.org/10.1016/j.geomorph.2013.06.015, 2013.

Monserrat, O. and Crosetto, M.: Deformation measurement using terrestrial laser scanning data and least squares 3D surface matching. ISPRS J. Photogramm., 63(1), 142–154, https://doi.org/10.1016/j.isprsjprs.2007.07.008, 2008.

Niculiţă, M.: Automatic landslide length and width estimation based on the geometric processing of the bounding box and the geomorphometric analysis of DEMs, Nat. Hazards Earth Syst. Sci., 16, 2021-2030, https://doi.org/10.5194/nhess-16-2021-2016, 2016.

Niethammer, U., S. Rothmund, M. R. James, Travelletti, J. and Joswig M.: UAV based remote sensing of landslides, Int. Arch. Photogram. Remote Sensing Spatial Info. Sci., 38(5), 496-501, 2010.

Petschko, H.; Bell, R. Glade, T.: Effectiveness of visually analyzing LiDAR DTM derivatives for earth and debris slide inventory mapping for statistical susceptibility modeling, Landslides 13(5), 857-872, 2016, https://doi.org/10.1007/s10346-015-0622-1.

Pike, R.J.: The geometric signature: quantifying landslide-terrain types from digital elevation models, Mathematical Geology, 20, 5, 491-511, 1988.

Plank, S.: Rapid damage assessment by means of multi-temporal SAR—A comprehensive review and outlook to Sentinel-1, Remote Sensing, 6, 6, 4870-4906, https://doi.org/10.3390/rs6064870, 2014.

607   Razak, K. A., Santangelo, M., Van Westen, C. J., Straatsma, M. W., and de Jong, S. M.: Generating an
608   optimal DTM from airborne laser scanning data for landslide mapping in a tropical forest
609   environment, Geomorphology, 190, 112-125, https://doi.org/10.1016/j.geomorph.2013.02.021, 2013.

610   Rosi, A., Vannocci, P., Tofani, V., Gigli, G., Casagli, N.: Landslide characterization using satellite
611   interferometry (PSI), geotechnical investigations and numerical modelling: the case study of Ricasoli
612   Village (Italy). Int. J. Geosci., 4, 904-918, https://doi.org/10.4236/ijg.2013.45085, 2013.

613   Santangelo, M., Cardinali, M., Rossi, M., Mondini, A. C., and Guzzetti, F.: Remote landslide mapping using
614   a laser rangefinder binocular and GPS, Nat. Hazards Earth Syst. Sci., 10, 2539-2546,
615   https://doi.org/10.5194/nhess-10-2539-2010, 2010.

616   Santangelo, M., Marchesini, I., Bucci, F., Cardinali, M., Fiorucci, F., and Guzzetti, F.: An approach to
617   reduce mapping errors in the production of landslide inventory maps, Nat. Hazards Earth Syst. Sci.,
618   15, 2111-2126, https://doi.org/10.5194/nhess-15-2111-2015, 2015a.

619   Santangelo, M., Marchesini, I., Cardinali, M., Fiorucci, F., Rossi, M., Bucci, F., Guzzetti, F. A method for
620   the assessment of the influence of bedding on landslide abundance and types. Landslides 12, 295–
621   309. doi:10.1007/s10346-014-0485-x, 2015b.

622   Tarchi, D., Casagli, N., Fanti, R., Leva, D. D., Luzi, G., Pasuto, A., Pieraccini, M., Silvano, S.: Landslide
623   monitoring by using ground-based SAR interferometry: an example of application to the Tessina
624   landslide in Italy. Eng. Geol., 68, 1, 15-30, https://doi.org/10.1016/S0013-7952(02)00196-5, 2003.

625   Teza, G., Galgaro, A., Zaltron, N., Genevois, R.: Terrestrial laser scanner to detect landslide displacement
626   fields: a new approach. Int. J. Remote Sensing, 28, 16, 3425-3446,
627   https://doi.org/10.1080/01431160601024234, 2007.

628   Torrero, L. Seoli, L. Molino, A. Giordan, D. Manconi, A. Allasia, P. and Baldo, M. The Use of Micro-UAV
629   to Monitor Active Landslide Scenarios, in: Engineering Geology for Society and Territory, edited by:
630   Lollino, G., Manconi, A., Guzzetti, F., Culshaw, M., Bobrowsky P., and Luino, F., Springer
631   International Publishing Switzerland, 5, 701-704, https://doi.org/10.1007/978-3-319-09048-1_136,
632   2015.

633   Turner, D.; Lucieer, A. de Jong, S. M.: Time Series Analysis of Landslide Dynamics Using an Unmanned
634   Aerial Vehicle (UAV), Remote Sensing 7(2), 1736-1757, 2015, https://doi.org/10.3390/rs70201736.

635   Van Den Eeckhaut, M., Poesen, J., Verstraeten, G., Vanacker, V., Nyssen, J., Moeyersons, J., van Beek, L.
636   P. H., and Vandekerckhove, L.: Use of LIDAR-derived images for mapping old landslides under
637   forest, Earth Surf. Proc. Land., 32, 754-769, https://doi.org/10.1002/esp.1417, 2007.

638

639

640

641 **Table 1.** Characteristics of the images used to identify and map the Assignano landslide (**Fig. 2**).

642 O: order in the sequence of images shown to the interpreter. Platform used to capture the image:

643 W, WorldView-2 satellite; U, UAV. Resolution (ground resolution), in metre. Spectral (image

644 spectral composite): TCC, True Colour Composite (Red, Green, Blue); FCC, False Colour

645 Composite (Near infrared, Red, Green). Type (image type): M, monoscopic; S, stereoscopic; P,

646 pseudo-stereoscopic. Map: Corresponding landslide map (**Fig. 5**).

647

O	Platform	Resolution	Spectral	Type	Map
1	W	1.84	TC	M	C
2	W	1.84	FCC	M	D
3	W	1.84	TC	S	E
4	W	1.84	FCC	S	F
5	U	0.03	TC	M	G
6	U	0.03	TC	P	H

648

649

650   **Table 2**. Comparison of the total landslide area (A_L), the landslide source and transportation area

651   (A_{LS}), the landslide deposit (A_{LD}), the width and length of the entire landslide (W_L, L_L), of the

652   source and transportation area (W_{LS}, L_{LS}), and of the deposit (W_{LD}, L_{LD}), for eight separate and

653   independent cartographic representations of the Assignano landslide. EL, entire landslide; ST,

654   landslide source and transport area; LD, landside deposit. See **Table 3** for the characteristics of the

655   single maps.

656

		Map A	Map B	Map C	Map D	Map E	Map F	Map G	Map H
Landslide area (m^2)									
EL	A_L	1.11×10^4	1.91×10^4	1.53×10^4	1.52×10^4	1.09×10^4	1.06×10^4	1.19×10^4	1.16×10^4
ST	A_{LS}	5.40×10^3	7.40×10^3	3.64×10^3	4.02×10^3	5.71×10^3	6.03×10^3	5.21×10^3	5.70×10^3
LD	A_{LD}	5.73×10^3	1.17×10^4	1.16×10^4	1.12×10^4	5.15×10^3	4.59×10^3	6.70×10^3	5.87×10^3
Landslide length (m) and width (m)									
EL	W_L	70.7	97.8	113.4	109.9	61.4	61.25	89.9	85.3
	L_L	362.0	387.5	404.7	391.2	354.6	359.5	343.3	349.1
ST	W_{LS}	51.5	59.6	43.6	49.2	51.92	54.3	49.5	50.5
	L_{LS}	227.9	229.7	205.9	208.0	239.0	239.2	234.7	237.3
LD	W_{LD}	61.0	98.69	111.5	109.0	56.0	57.6	89.9	81.9
	L_{LD}	152.7	172.1	206.2	203.5	129.8	134.7	139	121.8

657

658

659   **Table 3**. Comparison of the estimated cost, acquisition and pre-processing time, and storage

660   requirement for an area of 4 km^2 (2 km × 2 km) and for an area of 100 km^2 (10 km × 10 km), for

661   monoscopic and stereoscopic satellite images, and for an area of 15 km^2 for photographic images

662   captured by an UAV.

663

	Satellite monoscopic		Satellite stereoscopic		UAV	
	4 km^2	100 km^2	4 km^2	100 km^2	4 km^2	15 km^2
Acquisition cost (€)	1.500	1.500	3.500	3.500	1.000	3.000
Pre-processing cost (€)	50	50	50	50	250-300	3.000
Acquisition time (day/person)	7-60	7-60	7-60	7-60	1	4
Pre-processing time (hr/person)	1	1	1	1	5-6	20-24
Storage (GB)	0.5	0.5	1	1	12	50
Resolution (m)	2	2	2	2	0.02	0.02
Morphologic signature	no	no	yes	yes	yes	yes
Photographic signature	yes	yes	yes	yes	yes	yes

664

665

666

Figure captions

Figure 1. The Assignano landslide, located near Collazzone, Umbria, central Italy. (A) global view of the landslide. (B) detail of the landslide source area. (C) detail of the landslide transportation area. (D) detail of the landslide deposit. Base image obtained overlaying ("draping") the image on Google Earth™. Red line is the boundary of the landslide obtained using the RTK DGPS (benchmark).

Figure 2. Images used to map the Assignano landslide. (A) TC WordView-2 satellite image, (A-I) detail of the source area and (A-II) detail of the landslide deposit. (B) WordView-2 satellite image in FCC, (B-I) detail of the source area and (B-II) detail of the landslide deposit. (C) UAV monoscopic image and C-I a detail of the source area and C-II a detail of the deposition area.

Figure 3. Position of the seven GCPs used to evaluate the co-registration of WordView-2 satellite image (A) and UAV image (B). Corresponding points are illustrated with the same symbol. Differences of the coordinates of the corresponding points along X (i.e., E-W direction, ΔX) and along Y (i.e., N-S direction, ΔY) are provided in metres on the left of the figure.

Figure 4. (A) Overview of the Assignano landslide area in Google Earth™ taken on 8 July 2013. Photo shooting points and photograph taken (B) close to the landslide and (C) from a viewpoint.

The photographs taken in the field and the Google Earth™ image were used to prepare the reconnaissance field map.

Figure 5. Eight independent cartographic representations of the Assignano landslide, "Map A" to "Map H". Map A obtained through a RTK DGPS survey is considered the "benchmark", and shown as a thick black line in the other maps. Map B obtained through reconnaissance field mapping. Map C to Map F obtained through the expert visual interpretation of the satellite images. Map G and Map H obtained through the expert visual interpretation of the orthorectified image taken by the UAV. See **Table 1** for image characteristics. Dark colours show the landslide source and transportation area. Visual inspection of the images reveals the maps most similar to the benchmark.

**Figure 6**. The error index (*E*) proposed by Carrara et al. (1992), was used to compare quantitatively the different landslide maps. (I) Error index matrix for the landslide source and transportation area. (II) Error index matrix for the landslide deposit. (III) Error matrix for the entire landslide. *E* spans

696   the range from 0 (perfect matching) to 1 (complete mismatch).

697   **Figure 7**. Comparison of landslide maps prepared for the Assignano landslide, Umbria, Central

698   Italy. (A) Landslide map obtained from a monoscopic (Map C, dark yellow line) and a stereoscopic

699   (Map E, light blue line), true-colour (TC) WordView-2 satellite image (base image), and a mapping

700   of the landslide obtained by walking a GPS receiver along the landslide boundary (Map A, black

701   line). (B) Landslide map obtained from a monoscopic (Map D, yellow line) and a stereoscopic

702   (Map F, cyan line), false-colour-composite (FCC) WordView-2 satellite image, and a mapping

703   obtained by walking a GPS receiver along the landslide boundary (Map A, black line). (C)

704   Landslide map obtained from field survey (Map B, pink line) and from a monoscopic, TC, ultra-

705   resolution image captured by an UAV (Map G, purple line), and the mapping obtained by walking

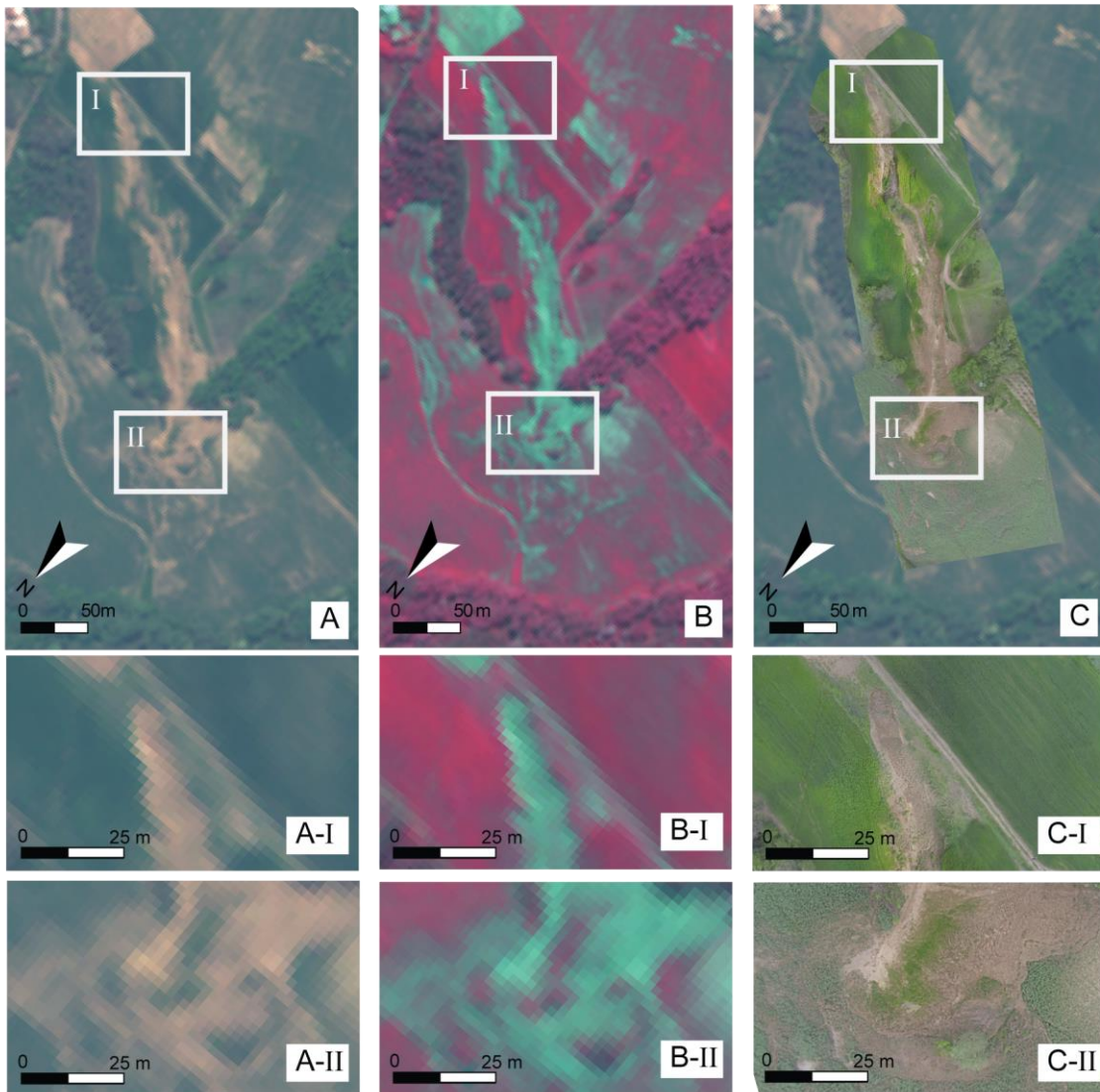706   a GPS receiver along the landslide boundary (Map A, black line).
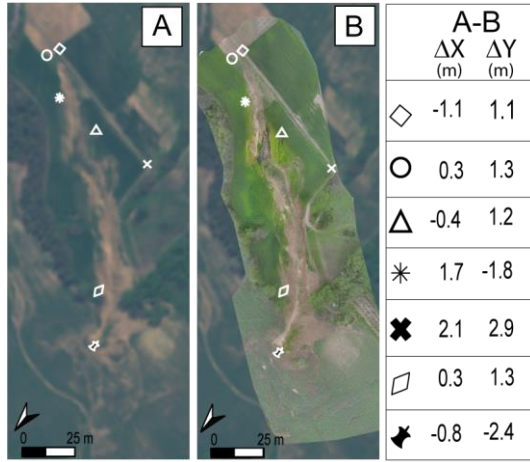
707

708   **Figure 1**
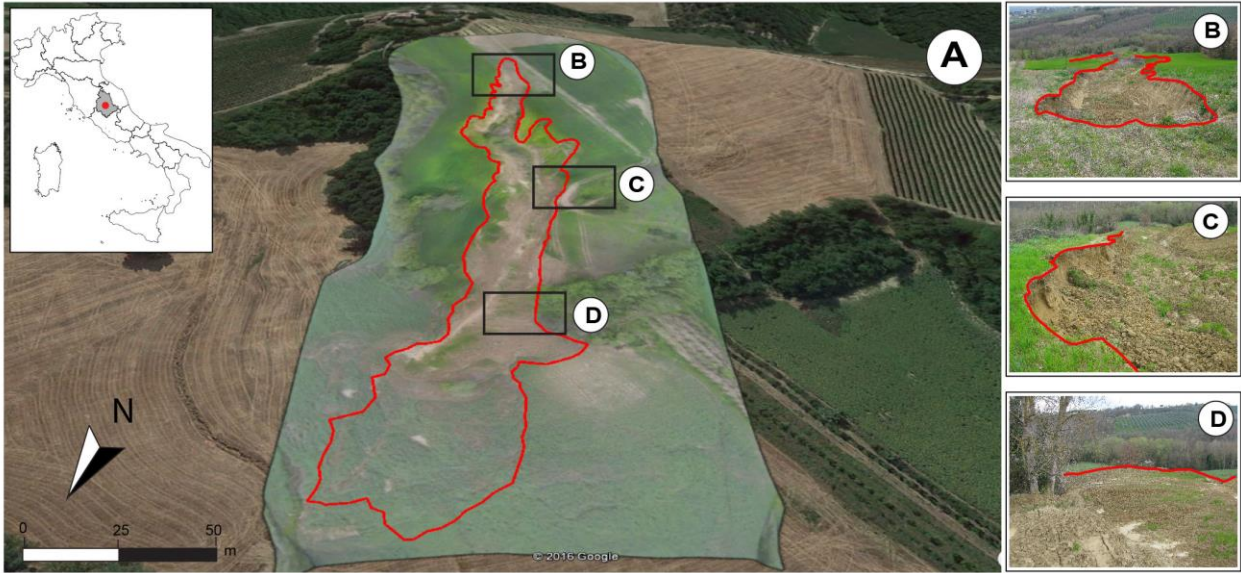
709

710

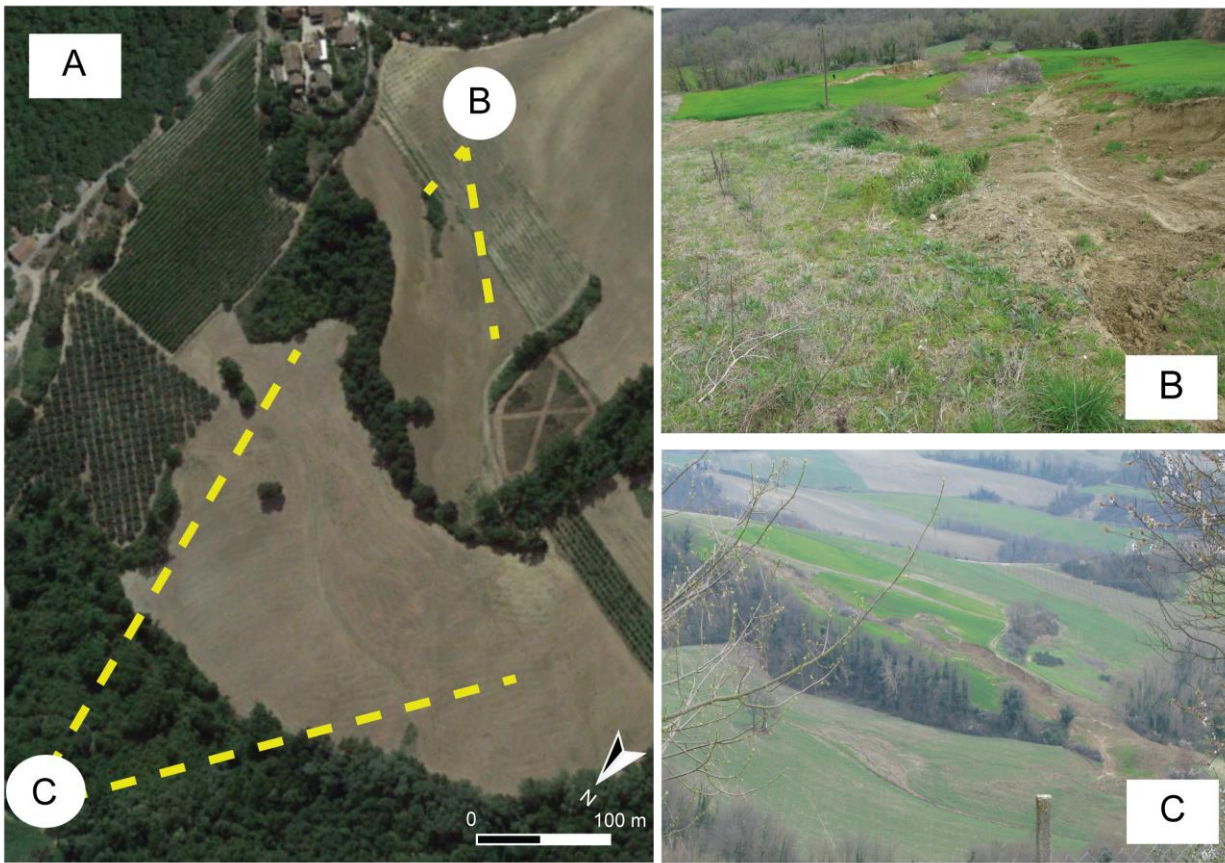711   **Figure 2**

712

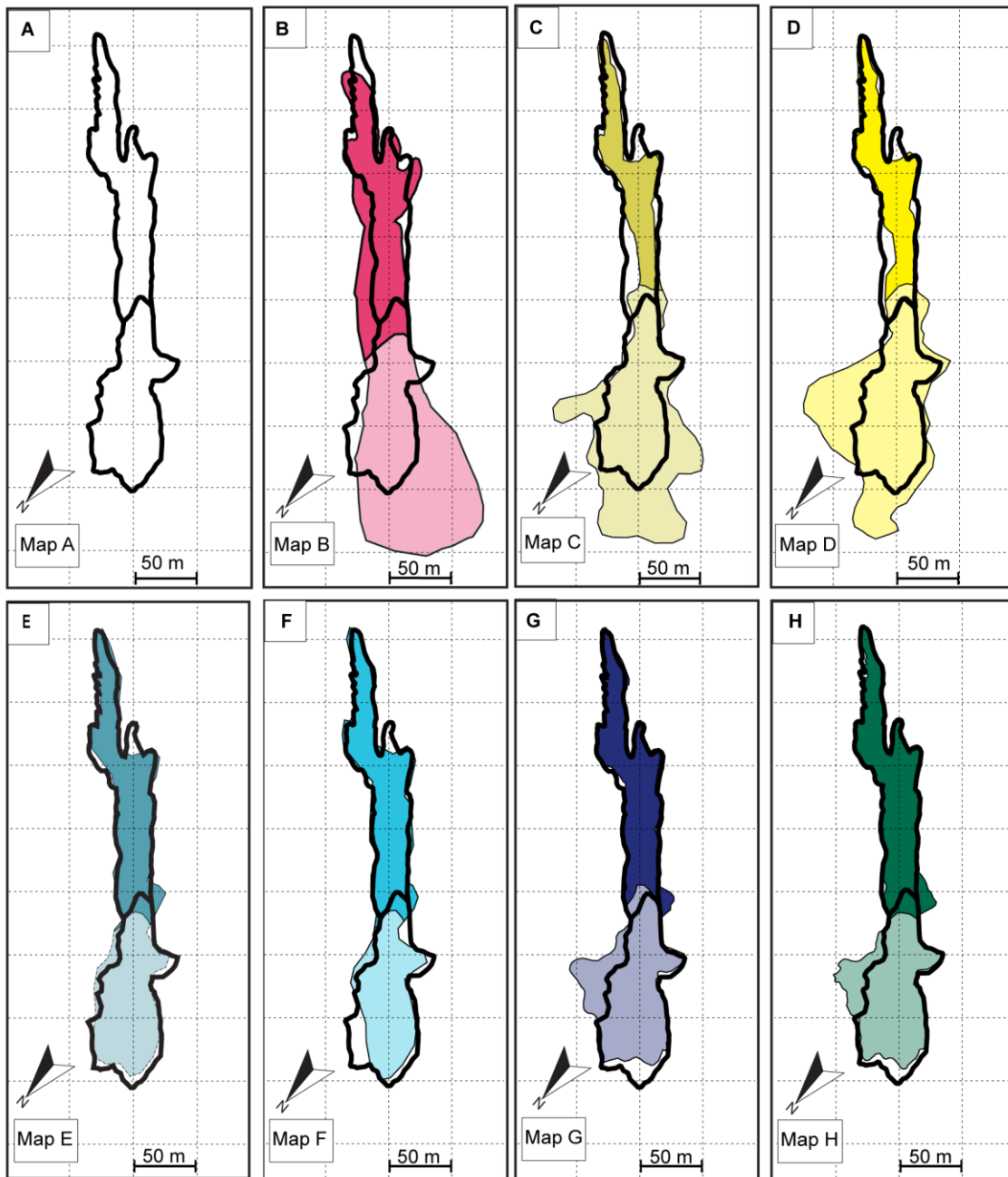713   **Figure 3**
714

715

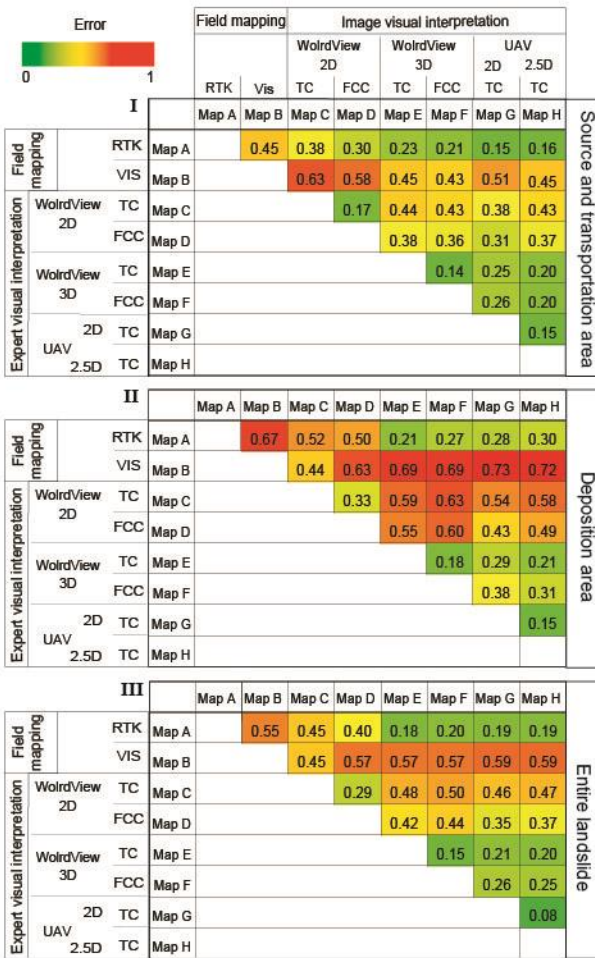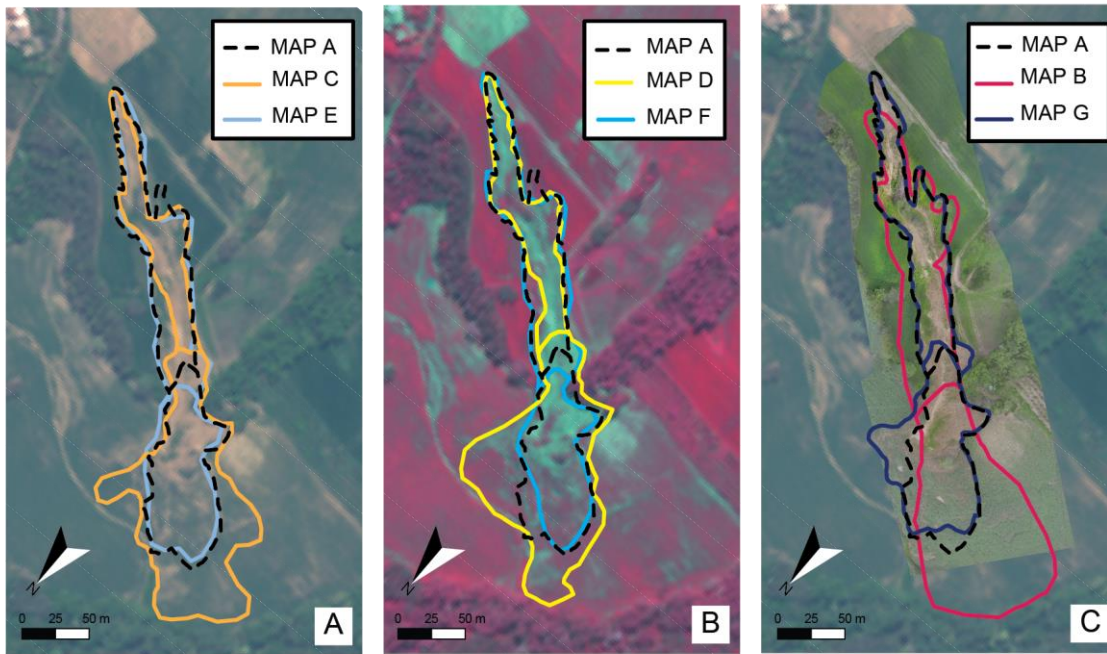716 **Figure 4**

717

718   **Figure 5**

719

720   **Figure 6**

721

722

723

724   **Figure 7**

725